Mechanism and Machine Theory 176 (2022) 104997

Contents lists available at ScienceDirect

Mechanism and Machine Theory

journal homepage: www.elsevier.com/locate/mechmt

Research paper

Development and test of a high speed pusher-type inchworm piezoelectric actuator with asymmetric driving and clamping configuration

Jie Ling [a,*], Long Chen [a], Zhao Feng [b], Yuchuan Zhu [a]

[a] College of Mechanical and Electrical Engineering, Nanjing University of Aeronautics and Astronautics, Nanjing 210016, China
[b] Faculty of Science and Technology, University of Macau, 999078, Macao Special Administrative Region of China

ARTICLE INFO

Keywords:
Piezoelectric actuator
Inchworm movement
Compliant mechanism
High-speed motion
Driving characteristic analysis

ABSTRACT

The pusher type inchworm piezoelectric actuator has the advantages of fast response and wide stroke, but the complex excitation signal sequences limits the output speed and load capacity. An asymmetric driving and clamping configuration along with simplified excitation signal sequences of a high speed piezoelectric actuator is proposed. A lever amplification mechanism is designed to increase the step. A hexagonal output shaft is designed to enhance the clamping force and the load capacity. The pseudo rigid body method is used to build the kinematic and statical model. Statics and dynamics are analyzed through both simulations and experiments. Results show that, when the driving voltage is 80 V, the maximum step is 71 μm at the driving frequency of 550 Hz, the maximum speed is 44.69 mm/s at the driving frequency of 650 Hz, the maximum clamp force is 432.2 N, and the maximum load is up to 60 g. Herein, the driving speed and load capacity are significantly improved compared with the traditional structures in the literature.

1. Introduction

The piezoelectric actuator (PSA) is widely used in many scientific and industrial fields, such as biomedicine [1–3], aerospace [4–6], precision manufacturing [7–10], etc. Piezoelectric actuators have the advantages of compact structure, large driving force, high resolution, low power consumption, which have attracted extensive attentions worldwide. Therefore, various kinds of piezoelectric actuators are designed and fabricated, such as direct-push type [11,12], ultrasonic type [13,14], stick–slip type [15–17] and inchworm type [18–21]. Direct-push type actuators are in high precision, but driving stroke is limited [11,12]. Ultrasonic type actuators have an unlimited stroke, but suffer from low life expectancy due to friction and wear [22]. Stick–slip actuators also have unlimited stroke, but strong loading capacity and high driving force are hard to obtain [15]. Inchworm actuators have unlimited stroke, good driving stability and repeatability, as well as excellent loading capacity, but it requires complex excitation signal sequences to produce clamping, feeding and releasing motions. This generally leads to limited driving frequency and speed [23].

The inchworm actuators can be generally classified into three categories, namely "walker" [19], "pusher", and "walker–pusher" [24]. A typical inchworm actuator is consisted of three parts, i.e., two clamping parts and a driving part. The operating principle of a "pusher" type and a "walker" type are shown in Fig. 1. As for a "pusher", the actuator itself is fixed and it pushes draft to move forward. As shown in Fig. 1(b), the operating process of a "pusher" is as follows: (1) the clamping part mechanism II extends to catch the draft tightly; (2) the driving part mechanism gets power and extends to make the draft get a forward displacement of

* Corresponding author.
E-mail address: meejling@nuaa.edu.cn (J. Ling).

https://doi.org/10.1016/j.mechmachtheory.2022.104997
Received 14 November 2021; Received in revised form 7 May 2022; Accepted 12 June 2022
Available online 24 June 2022

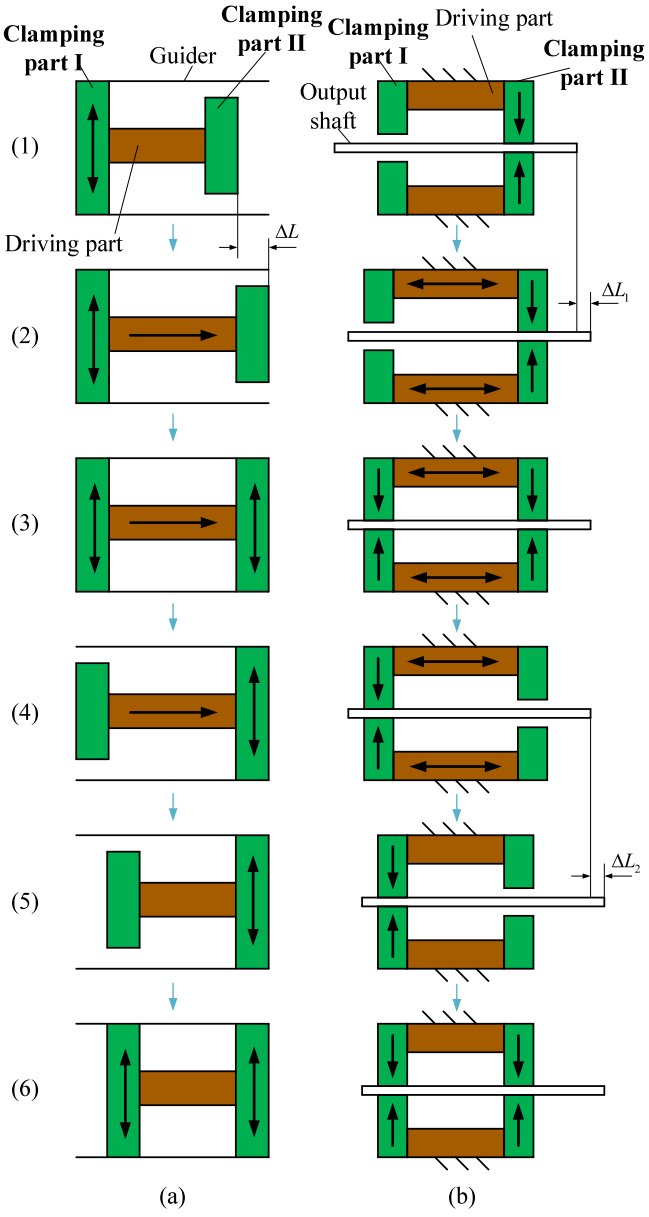

Fig. 1. Operating principle of piezoelectric inchworm actuators. (a) "Walker" type. (b) "Pusher" type.

ΔL_1; (3) the clamping part mechanism I extends to hold the draft; (4) the clamping part mechanism II loses power and releases the draft; (5) the driving part mechanism extracts to its original state, the clamping part mechanism I brings the draft forward, and the displacement is marked as ΔL_2; (6) the clamping part mechanism I gets power again to hold the guider, and then the actuator goes into another cycle. The step size of "pusher" is calculated as $\Delta L = \Delta L_1 + \Delta L_2$. It can be seen that, both the contraction and extension of the driving part mechanism in a "pusher" make the draft move forward. Therefore, the draft moves twice in a cycle. It can be seen that driving sequences for each clamping and driving mechanism are complex mainly due to its structural configuration.

The complex structural configuration with clamping and driving mechanism leads to complex excitation signal sequences. The influence of excitation signal sequences on the output performance has been investigated in some works. The excitation signal sequences should ensure the clamped mechanism have enough overlapping time, otherwise the mover will become freedom and lose driving ability instantaneously, i.e., the load capacity will be deteriorated [24]. It is also pointed in [18] that the phases among the excitation signal sequences need to be adjusted to adapt to the different response characteristics of driving and clamping mechanisms, so as to avoid unstable motion caused by mechanical crawling. Some efforts have been made to improve the performances of the pusher-type inchworm actuators. To simplify the excitation signals, a piezoelectric inchworm actuator driven by one channel DC signal is presented in [18]. The output step is achieved as 0.241 μm under no-load conditions at a voltage of 75 V and frequency of

3.2 Hz. An inchworm actuator using a compound mechanism of lever amplifier and bridge amplifier is developed in [19], where the motion is realized through the cooperation of an amplification mechanism and an elastomer. The obtained output speed of this actuator is 0.72 mm/s at a driving frequency of 50 Hz. A self-adapting linear inchworm piezoelectric actuator is reported in [20] to improve the driving stability, and the maximum output force is obtained as 15 g with a resolution of 0.03 μm under a driving frequency at 40 Hz. An inchworm actuator with only two pieces of piezoelectric ceramics is proposed in [21]. The structure is simplified a lot by utilizing the lateral deformation and its associated motion to realize the clamping and driving functions. The output speed of this actuator is achieved as 0.216 mm/s at a driving frequency of 20 Hz. Most of the efforts focus on the optimization of the structures [19,20] or the simplification of the excitation signal sequences [18,21].

However, driving speed is a major performance index of a piezoelectric actuator. Due to the complicated excitation signal sequences and low natural frequency of compliant mechanism, which leads to limited driving frequency, the speed of the actuator, which is calculated as $v = \Delta L \cdot f$, is small. Although some works have attempted to simplify the excitation mode [18,21], for some applications, such as a variable airfoil aircraft, these actuators cannot meet either the output step or the speed. Novel configurations of the inchworm actuators with an output step at dozens of microns and a speed at dozens of millimeters per second need to be investigated.

In order to increase the speed of piezoelectric inchworm actuators, an improved pusher-type structure of asymmetric driving and clamping configuration along with simplified excitation signal sequences of a high speed piezoelectric actuator is proposed in this paper. The driving mechanism based on lever amplifier have a large amplification ratio to obtain a better forward displacement ΔL. Besides, a hexagon draft is used to increase contact area for larger clamping force. Therefore, the superiority of the proposed driving method is three-fold: (1) larger step size to achieve a better speed performance; (2) simplified excitation mode with less driving sequences in one period; (3) large clamping force to obtain a stable and smooth driving performance and high load capacity. The contributions of this work can be summarized as:

- An asymmetric driving and clamping configuration is proposed to simplify the excitation mode.
- The kinematic and statical models of the actuator are established for the designers to conduct performance analysis as well as optimization.
- Both simulations and experiments are performed to support the superiority of the proposed actuator with comparisons with some existing prototypes.

The rest of the paper is arranged as follows. Configuration and operating principle of the proposed piezoelectric inchworm actuator are introduced in Section 2. The kinematic and statical modeling process and the analysis are explicated in Section 3. In Section 4, finite element model is built for simulation to test the performance of the actuator. Experimental validations are presented in Section 5. Discussions on pros and cons of the design are made in Section 6. Finally, the paper is concluded in Section 7.

2. Configuration and operating principle

In this section, the configuration and operating principle of the proposed "pusher" type piezoelectric inchworm actuator are introduced.

2.1. Structural configuration

As show in Fig. 2(a), the proposed pusher-type piezoelectric inchworm actuator is composed of a compliant driving mechanism, six PSAs (A_1, A_2, B_1, B_2, C_1 and C_2), an octagon shaft, pre-load screws, gaskets, etc. The upper half and the lower half of the driving mechanism are symmetrical. The compliant driving mechanism is mounted on vibration isolation table with screws. The shaft is installed on the driving mechanism.

The driving mechanism is divided into three parts: driving part, clamping part I and II, as shown in Fig. 2(b). The compliant driving mechanism is consisted of rigid links, rotational flexure hinges, fixing holes, PSA installation grooves, pre-loading screws, etc. The compliant driving mechanism has a unitary and compact structure, which makes it easy to fabricate. Overall size of the proposed piezoelectric actuator is 110 mm× 106 mm× 10 mm. As zoomed in the figure, the flexure hinge is of great importance to transmit the motion via small deformation. Three parameters need to be designed, i.e., the radius r, the height h, and the thickness t. This will be discussed in the following sections.

2.2. Working principle

As presented in Fig. 1, in a traditional push-type inchworm actuator, the clamping part I and clamping part II have the same function, i.e., to clamp the output shaft at the expanding stage of the driving part such that a stepping motion can be produced. In one cycle, the driving part expands twice (denoted as l for each expanding length) and produces a stepping stroke of half of its expanding length for each time (i.e., $\Delta L_1 = \Delta L_2 = 0.5l$) due to the left–right symmetry structure, thus the total stepping stroke for each period will be $\Delta L_1 + \Delta L_2 = l$ without consideration of deformation loss. However, such a kind of excitation mode requires complex excitation signal sequences to produce two expanding stages of the driving part and four clamping stages of the clamping part. The requirements of the control system are extremely high for such excitation mode, especially for high driving frequencies.

To simplify the excitation signal sequences and to improve the stepping stroke simultaneously, a left–right asymmetry structure is utilized in the proposed actuator. As shown in Fig. 3, the driving part and the clamping part II are fixed together with no relative

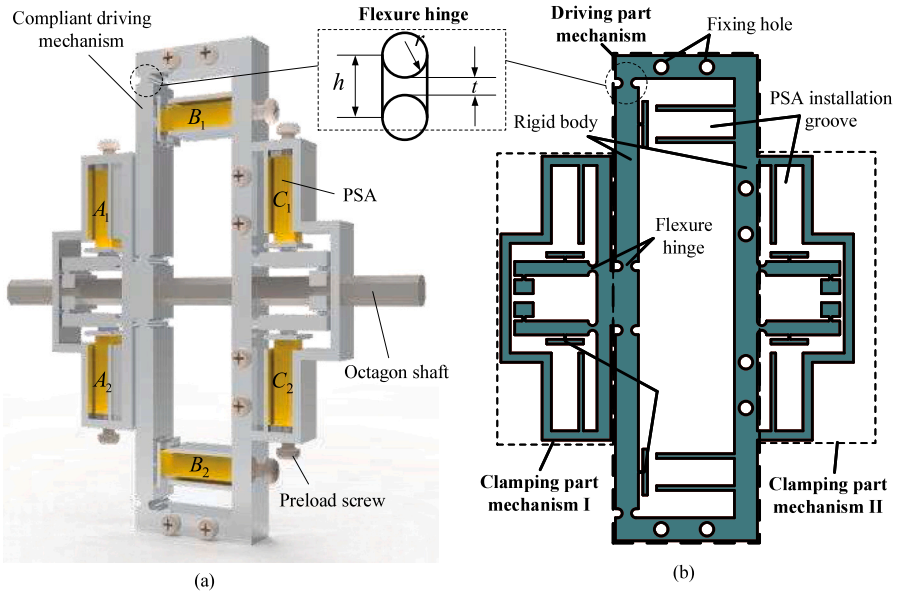

Fig. 2. Three-dimensional model and compliant driving mechanism of the proposed piezoelectric inchworm actuator.

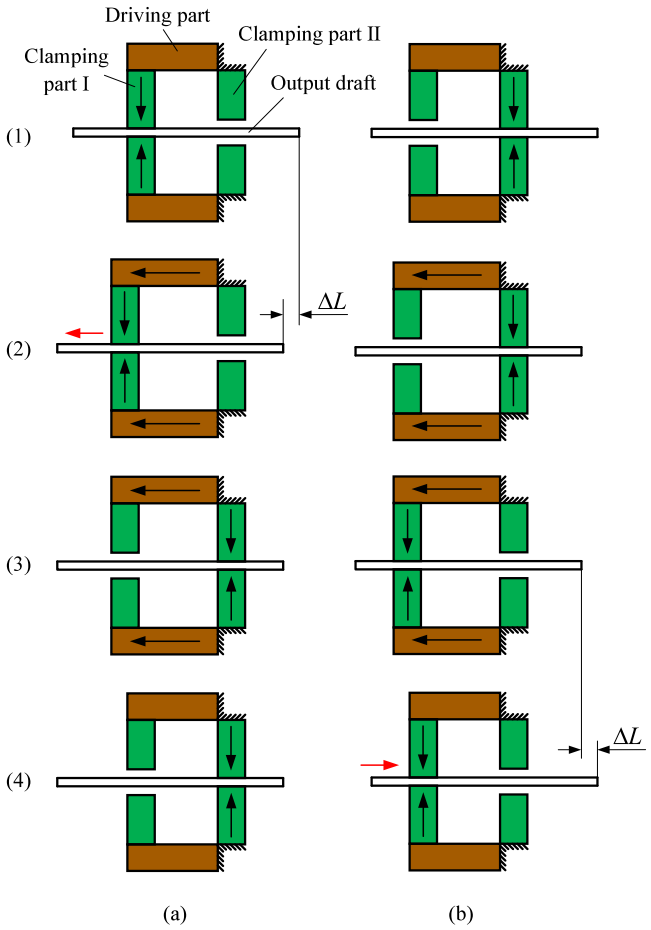

Fig. 3. Operating principle of the proposed "pusher" type piezoelectric inchworm actuator. (a) Driving direction is left. (b) Driving direction is right.

Table 1
Working state of each part of compliant driving mechanism in a cycle.

Driving direction	Part	t_1	t_2	t_3	t_4
Left	Clamping part I	+	++	–	––
	Driving part	––	+	++	–
	Clamping part II	–	––	+	++
Right	Clamping part I	-	––	+	++
	Driving part	––	+	++	–
	Clamping part II	+	++	–	––

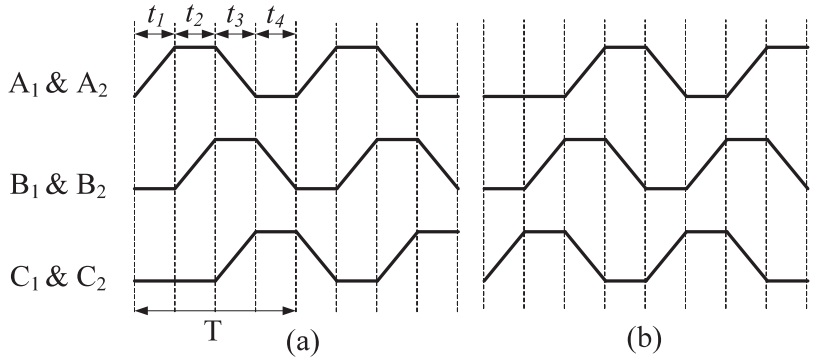

Fig. 4. Driving signals of the proposed inchworm actuator. (a) Driving direction is left. (b) Driving direction is right.

movement between each other. The function of clamping part I is to clamping the output shaft and then to drive it to produce stepping motion, while the clamping part II is designed to clamping the output shaft at the reset stage of the driving part to prevent return stroke.

The operating principle of the proposed push-type piezoelectric inchworm actuator in two directions is shown in Fig. 3. Different from the traditional push-type inchworm actuator, the shaft only moves once in each cycle due to asymmetric structure of the driving mechanism. The operating principle of the proposed inchworm actuator is as follows:

(a) The driving direction is left. (1) The clamping part I expands to hold the shaft. (2) The driving part extends to drive the shaft to move left. (3) The clamping part II clamps the draft, and clamping part I releases. (4) The driving part then extracts to the original state. After that, the clamping part I clamps the draft again, and the clamping part II releases for next cycle.

(b) The driving direction is right. (1) The clamping part II holds the draft. (2) The driving part gets power to extend. (3) The clamping part I extends to hold the draft and the clamping part II loses contact to the draft. (4) The driving part loses power to get back to its initial state and driving the draft to move right. Then the clamping part II extends to hold the draft and the clamping part I releases for next coming cycle.

Compared with the operating principle of a traditional push-type inchworm actuator, it can be found that, the features of the proposed actuator lie in: (1) The excitation signal sequences in one cycle are reduced so that the excitation mode is simplified; (2) Although only one step is generated in one cycle for the new actuator, the final stepping stroke is $\Delta L = l$ providing that the driving voltage for the piezo stack is the same with that of the traditional actuator. Hence, the output step is not decreased due to the modification of the structural configuration. In addition, with the proper design of a lever amplification mechanism, the output step can be increased according to the driving requirements.

2.3. Excitation mode

According to the operating principle above, the corresponding excitation signal sequences for each PSA (i.e., the stacks marked as A_1, A_2, B_1, B_2, C_1, C_2 in Fig. 2(a)) are proposed in this subsection. There are four working states of each part of the actuator as shown in Table 1, where "++" denotes power-on state, "––" denotes power-off state, "+ " denotes voltage increasing stage, and "–" denotes voltage decreasing stage. Input signals applied to each PSA is a trapezoidal wave with a period of T, as shown in Fig. 4. It can be seen that the wave shape of driving signal of each PSA is same in both driving directions.

3. Compliant mechanism design and analysis

In this section, a pseudo-rigid-body model of the proposed compliant driving mechanism based on lever amplifier is built for motion analysis, force analysis and modal analysis. The movement characteristics are obtained and the structural parameters are optimized.

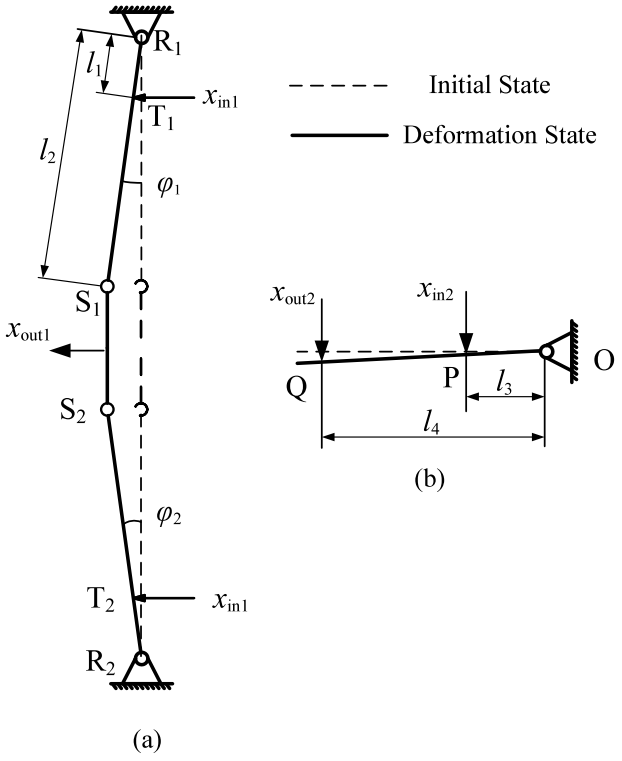

Fig. 5. Kinematics model of the proposed compliant driving mechanism based on lever amplifier. (a) The driving part. (b) The clamping part.

3.1. Kinematics analysis

Applying the pseudo-rigid-body method, the kinematic model of the driving mechanism can be built as shown in Fig. 5(a). The driving part is composed of three rigid links (i.e., R_1S_1, S_1S_2, and R_2S_2), and four rotational flexure hinges (i.e., R_1, R_2, S_1, and S_2). T_1 and T_2 are marked as the points where the PSAs of A_1 and A_2 output displacements. The driving part is a upper–lower symmetric structure. Therefore, the following relationships can be obtained,

$$\varphi_1 = \varphi_2 \tag{1}$$

$$x_{out1} = x_{in1}\frac{l_2}{l_1} \tag{2}$$

where φ_1 and φ_2 denotes the deflection angles between the rigid links of R_1S_1 and R_2S_2 with the vertical direction. l_1, l_2, l_3 and l_4 are the length of the corresponding links. x_{in1} is the output displacement of the PSA, and x_{out1} is the output displacement of the driving part. Hence, the displacement amplification ratio R_D of driving mechanism can be calculated as,

$$R_D = \frac{l_2}{l_1}. \tag{3}$$

As for the clamping part in Fig. 5(b), it is consist of a rigid link OQ and a flexure hinge O. Point P is marked as the displacement output location of the PSA B_1. Then, the output displacement can be calculated as,

$$x_{out2} = x_{in2}\frac{l_4}{l_3} \tag{4}$$

where L_3 denotes the length of rigid link C_1G_1; l_4 denotes the length of rigid link C_1H_1; x_{out1} is the output displacement of the clamping part.

3.2. Statics analysis

The rigid link is decomposed as shown in Fig. 6 to analyze the force and the moment of force. For the two PSAs (A_1 and A_2), the output forces are the same at the measurement points of T_1 and T_2 when the input voltages are the same, i.e., $F_{in1} = F_{in2}$. These two forces are then transmitted to drive the compliant hinge to rotate.

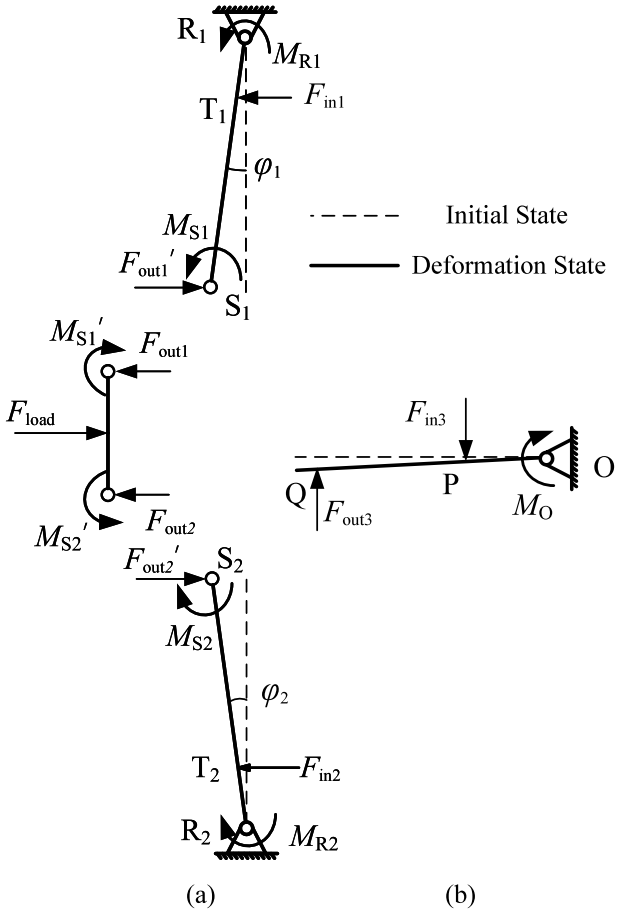

Fig. 6. Force analysis of compliant driving mechanism. (a) The driving part. (b) The clamping part.

For the rigid links R_1S_1 and S_1S_2, the force balance and the moment of force balance relationships can be obtained as,

$$M_{R1} + M_{S1} + F'_{out1} l_2 - F_{in1} l_1 = 0 \tag{5}$$

$$M'_{S2} - M'_{S1} + F_{load} \cdot \frac{1}{2} l_{S_1S_2} - F_{out2} l_{S_1S_2} = 0 \tag{6}$$

$$F_{load} = F_{out1} + F_{out2} \tag{7}$$

where, M_{R1}, M_{S1} and M_{S2} are the moment of force at the corresponding points, F_{load} is the load of the mechanism, F_{out1} and F_{out2} are the output forces of the hinges at the measurement point of S_1 and S_2 respectively, F' represents the relative force of F.

As shown in Fig. 6(a), considering that the driving part is upper–lower symmetric, it can be obtained as,

$$F_{out1} = F_{out2} \tag{8}$$

Denote K_{R1} and K_{S1} as the rotational stiffness of the hinge R_1 and S_1 respectively, then it can be calculated as,

$$\begin{cases} M_{R1} = K_{R1}\varphi_{R1} \\ M_{S1} = K_{S1}\varphi_{S1} \end{cases} \tag{9}$$

where φ_{R1} and φ_{S1} are the deflection angles of the joint R_1 and S_1. Design the joint R_1 the same as joint S_1, then $K_{R1} = K_{S1} = K$. In addition, as the upper–lower symmetric structure, then the rotational stiffness of the hinge R_2 and S_2 are also the same as K.

Then, the statics of the upper component of the driving part can be obtained as,

$$\begin{cases} M_{R1} = \frac{1}{2} F_{in1} l_1 - \frac{1}{4} F_{load} l_2 \\ \varphi_{R1} = \frac{1}{K_1}(\frac{1}{2} F_{in1} l_1 - \frac{1}{4} F_{load} l_2) \\ x_{out1} = \frac{l_2}{K_1}(\frac{1}{2} F_{in1} l_1 - \frac{1}{4} F_{load} l_2) \\ \delta_{max1} = \frac{M_{R1}}{W_{z1}} \end{cases} \tag{10}$$

where, δ_{max1} represents the maximum tension and compression stress obtained at the thinnest point of the hinge, W_{z1} is the bending modulus of the hinge at its thinnest point.

As for the upper component of the clamping part, the pseudo rigid body model and its force analysis are shown in Fig. 6(b). Denote point P to detect the output force of the PSA and the point Q as the contact point between the clamping mechanism and the output shaft. The force relations can be obtained as,

$$\begin{cases} F_1 l_1 - F_2 l_2 = 0 \\ F_1 - F_{oy} - F_2 = 0 \end{cases} \tag{11}$$

where, F_1 is the output force of the PSA, F_2 is the clamping force which is preload on the output shaft. l_1 and l_2 are the length of the link OP and OQ. F_{oy}. Therefore, the clamping force amplification ratio R_F can be calculated as,

$$R_F = \frac{F_2}{F_1} = \frac{l_1}{l_2}. \tag{12}$$

3.3. Dynamics analysis

When the PSA outputs force and displacement on the driving mechanism, the rigid links will be deflected, generating kinetic and potential energy. According to Lagrange's equation, the dynamics of the system can be expressed as,

$$\frac{d}{dt}\left(\frac{\partial T}{\partial \dot{q}_i}\right) - \frac{\partial T}{\partial q_i} + \frac{\partial V}{\partial q_i} = F_i, \quad i = 1, 2, \ldots, n \tag{13}$$

where, T and V represent the total kinetic energy and potential energy of the system, q_i is the generalized coordinate, n is the number of generalized coordinates, F_i represents the generalized nonconservative force [25].

Considering the upper component of the driving part as shown in Fig. 6, the total kinetic energy of the system can be expressed as,

$$T = J_{RS}\omega_{RS}^2 + \frac{1}{2} m_{S_1S_2} v_{S_1S_2}^2 + 2J_{OQ}\omega_{OQ}^2 \tag{14}$$

where, J_{RS} and ω_{RS} are the moment of inertia and the angular velocity of the rigid link R_1S_1 against the hinge R_1, $m_{S_1S_2}$ and $v_{S_1S_2}$ are the mass and the velocity of the rigid link R_1S_1, J_{OQ} and ω_{OQ} are the moment of inertia and the angular velocity of rigid link OP with respect to the hinge O.

The potential energy of the system can be expressed as,

$$V = K(\varphi_R^2 + \varphi_S^2) + 2K_O\varphi_O^2 \tag{15}$$

where K is the rotational stiffness of the hinge as described in Eq. (19), K_O and φ_O are the rotation stiffness and the rotation angle of the joint O, respectively.

Finally, the dynamic model of the upper component of the driving part can be derived as,

$$M\ddot{x}_{in} + Kx_{in} = F \tag{16}$$

with

$$\begin{cases} M = \frac{2J_{RS}}{l_2^2} + \frac{4J_{OQ}}{l_4^2} + m_{S_1S_2} \\ K = \frac{2K_1}{l_2^2} + \frac{4K_O}{l_4^2} \\ F = F_{in1} + F_{in2} - F_{load} \end{cases} \tag{17}$$

The natural frequency of the system can then be obtained as,

$$f = \frac{1}{2\pi}\sqrt{\frac{K}{M}}. \tag{18}$$

3.4. Parameter optimization

According to the above analysis, structural parameter determination as well as the optimization can be carried out to obtain the design objective. As listed in Table 2, parameters for the driving and clamping mechanisms are chosen according to the kinematics and statics analysis to obtain designed magnification ratio of the displacement or force. This will be evaluated in the simulations and experiments.

Working bandwidth is important for the actuator to produce high speed stepping motion [25]. For this case, the radius r and the thickness t of flexure hinge in the compliant driving mechanism are set as the optimization objects as shown in Fig. 2. The goal is to achieve high working bandwidth, i.e., the natural frequency of the system in Eq. (18). The constraint condition is then set as,

$$s.t. \begin{cases} \delta_{max1} < [\sigma]/n_s \\ 1\ \text{mm} < t < 2\ \text{mm} \\ 1\ \text{mm} < r < (h-t)/2 \\ 1\ \text{mm} < h < 5\ \text{mm} \end{cases} \tag{19}$$

Table 2
Design parameters of the compliant mechanism.

Driving mechanism		Clamping mechanism		Flexure hinge	
Parameters	Value	Parameters	Value	Parameters	Value
l_1	10 mm	l_3	7 mm	t	1.5 mm
l_2	40 mm	l_4	16 mm	r	1.5 mm
R_F	0.25	R_F	0.4375	h	4.5 mm
R_D	4	R_D	2.2857		

Table 3
The first six natural frequencies of the proposed compliant driving mechanism.

Order	Natural frequency	Order	Natural frequency
1	722.07 Hz	4	2029.7 Hz
2	953.92 Hz	5	2312.6 Hz
3	1002.8 Hz	6	2470.4 Hz

where $[\sigma]$ is the allowable stress of the material used in the mechanism, n_s is safety factor which is set as 2.

Using MATLAB parameter optimization toolbox, set the initial value of the parameters as $[t,\ r] = [1,\ 1]$ (unit: mm), the optimized results of the parameters can be obtained as in Table 2. Note that $h = 2r + t$.

Remark 1. For the geometric parameters of driving and clamping mechanisms, they can be linearly calculated once the input and output strokes are determined. In this work, the two parameters for the flexure hinge are nonlinear to the achievable working bandwidth according to Eq. (13)~Eq. (18). Herein, we emphasize on the optimization of t and r. For the constraint conditions, tradeoff between the compliance and the fabrication difficulty is considered as: (1) the minimum values of r and t are set as 1 mm, (2) the maximum value of h is set as 5 mm.

4. Finite element analysis

In this section, the finite element model of compliant driving mechanism in inchworm thrust piezoelectric actuator is established to analyze its kinematic/mechanical characteristics. It can provide guidance for the subsequent experiments. Firstly, the vibration mode and modal analysis are carried out, then the displacement amplification ratio of the driving mechanism under different input displacements is analyzed by statics simulations. Then the transient dynamic analysis is carried out and the clamping force of the driver is preliminary tested.

4.1. Simulation setup

The finite element model of the actuator is established in ANSYS Workbench software environment. A fixed constraint was imposed on the fixed hole of the compliant driving mechanism, the contact condition between the driving mechanism and the output shaft was set as friction, and the friction coefficient was set as 0.2. The material of the compliant driving mechanism and the output shaft was chosen as 65Mn. The material density is 7800 kg/m^3, the Young modulus is 210 GPa, and the Poisson's ratio is 0.3.

4.2. Modal analysis

Modal analysis is used to determine the vibration characteristics of the actuator, i.e., the natural frequency and the vibration mode. In the modal analysis, fixed constraints were applied to the compliant driving mechanism at the fixed hole, and the first 6th order natural frequencies were obtained as shown in Table 3 with the first vibration mode displaced in Fig. 7. It can be seen that the first-order natural frequency of the system is 722.07 Hz, therefore the driving frequency is limited within this range in the experimental tests.

4.3. Displacement analysis

In the statics simulations, the displacement output of the corresponding driving signal of the PSA was loaded directly to the compliant driving mechanism to test the driving displacement amplification ratio. Since the maximum output displacement of the piezoelectric stack selected in the subsequent experimental tests is 20 μm, the input displacement range applied to the driving part of the compliant driving mechanism is set as 1~20 μm in the simulations. A displacement probe is added to the end of the output shaft to detect its output displacement as shown in Fig. 8.

The comparisons between simulation results and theoretical results are shown in Fig. 9. The driving displacement amplification ratio obtained by simulation is 3.753, which is slightly smaller than that of the theoretical result 4.0. The reason is the elastic deformation of mechanism is not considered in the theoretical analysis.

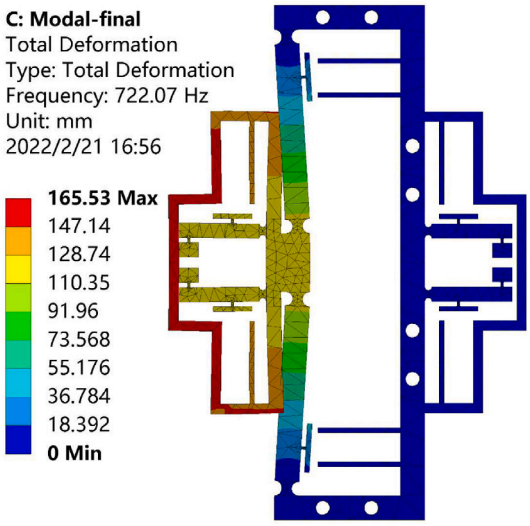

Fig. 7. The first vibration mode of the proposed compliant driving mechanism.

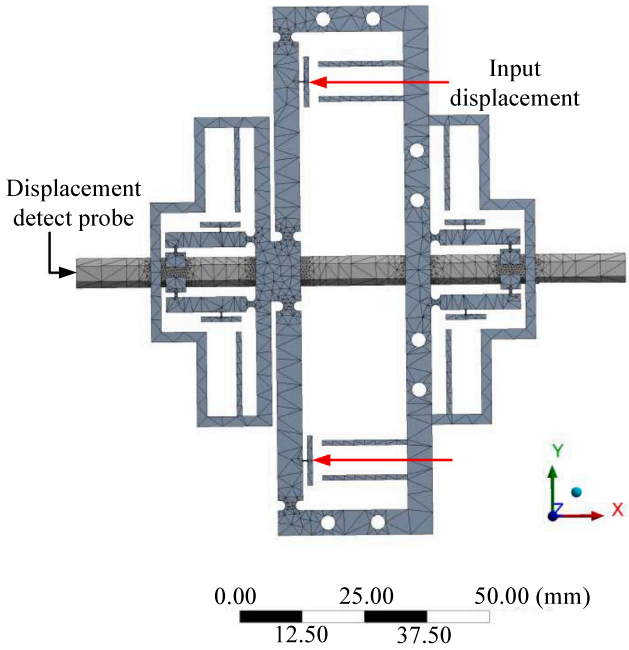

Fig. 8. Simulation environment settings in test of amplification ratio of driving mechanism and clamping.

4.4. Clamping force analysis

According to Eq. (12), the clamping force of C_1 or C_2 is proportional to the corresponding output force of the piezoelectric stack A_1 or A_2. In this section, the relationship between the clamping force and the input force was tested by a set of statics simulation.

Since the maximum output force of the piezoelectric stack is planned to be 1000 N in the subsequent experimental tests, the input force range is set as 0–1000 N in the simulations, which is loaded on the clamping part of the compliant driving mechanism. As shown in Fig. 10, a reaction force probe is added to the upper part of the output shaft in contact with the clamping part. The combined force of the three probes in the Y direction is then the clamping force.

The comparisons between the simulation and theoretical results of clamping force are shown in Fig. 11. It can be seen that the simulation clamping force amplification ratio is 0.4322, and the error between the simulation and theoretical results is 1.21%, which

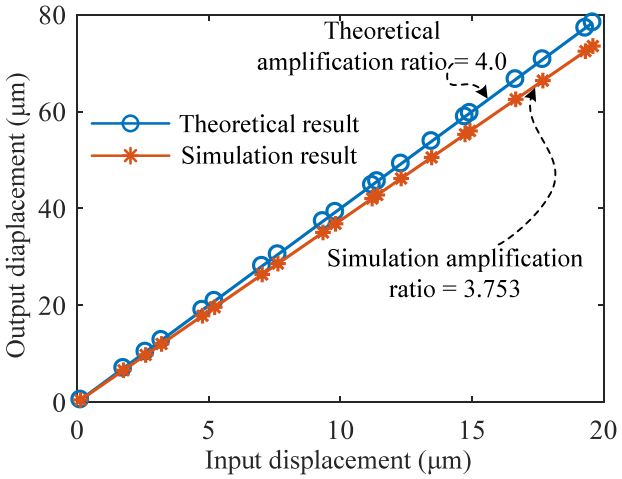

Fig. 9. Comparisons of output displacement between simulation and theoretical computation.

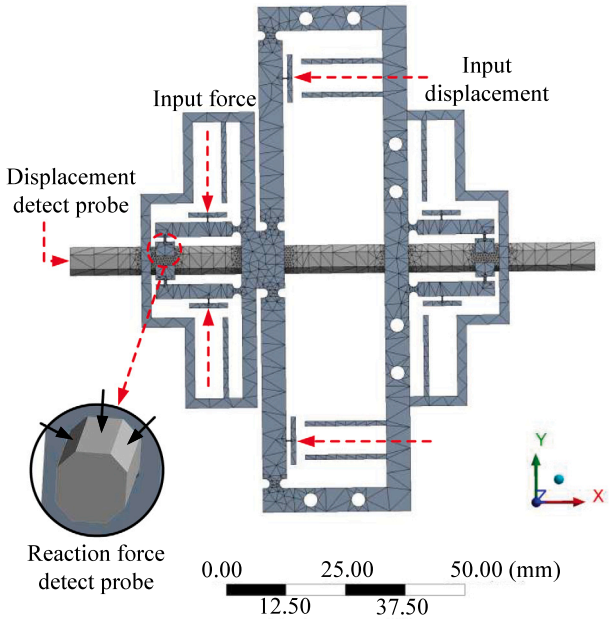

Fig. 10. Simulation environment settings in test of clamping force.

implies that the results are in good agreements with each other. Then, the maximum clamping force of the clamping mechanism can be further calculated as 432.2 N assuming that the maximum input force is 1000 N for the selected piezo stack.

5. Experimental results

In this section, according to the final parameters obtained from theoretical and simulation analysis, a prototype is designed and manufacture. The test platform is built, and the kinematic/mechanical properties of the proposed mechanism are evaluated.

5.1. Equipment setup

The prototype test system is shown in Fig. 12(a), where the Host PC generates control command signal and the real-time controller (model: RT-Links Box 03) outputs 0–5 V analog voltage signal in the target PC. The signal serves as the input of the power amplifier (model: AETechron 7224). After 16 times of amplification, the output of 0–80 V analog voltage signal is generated to drive the piezoelectric stack (model: Harbin Chip TECHNOLOGY RP150/5 × 5× 18).

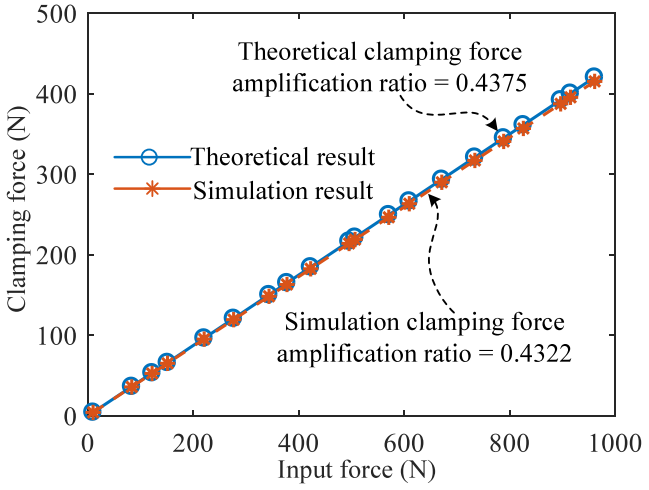

Fig. 11. Comparisons of clamping force between simulation and theoretical computation.

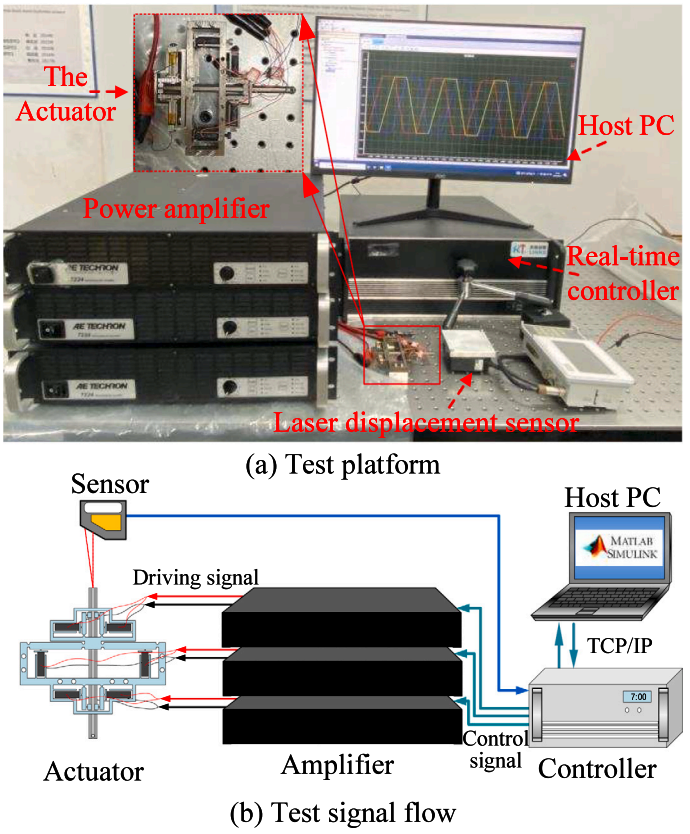

Fig. 12. Test platform of the proposed pusher-type piezoelectric inchworm actuator.

The stepping displacement of the piezoelectric actuator is measured by a laser displacement sensor (Model: OPTEX CD33-120N(P)-422), and is collected, recorded and then stored in the target PC. The signal flow of this process test system is shown in Fig. 12(b).

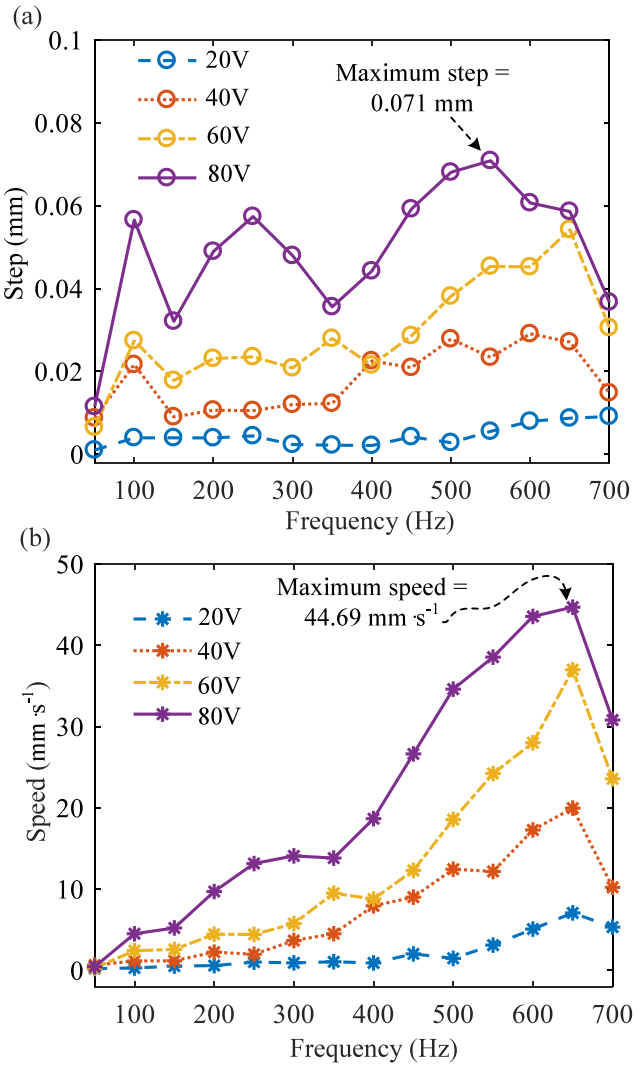

Fig. 13. Test results of step size and speed under different driving frequencies. (a) Step results. (b) Speed results.

5.2. Step and speed

The step of the actuator refers to the displacement of the output shaft in one driving cycle, and its value is related to the frequency as well as the amplitude of the driving signal. The first-order natural frequency of the system obtained from the above simulation is 722.07 Hz. Therefore, the frequency range of the driving signal is set as 0~700 Hz in the tests here, and the amplitude of the driving voltage is set as 20–80 V. The test results of the step distance and speed are shown in Fig. 13.

According to Fig. 13(a), it can be seen that,

(i) Due to the frictions of clamping part against the output shaft, the driving force of the piezoelectric stack output needs to overcome static friction force and dynamic friction force to drive the driving mechanism. Therefore, the steps under different driving voltage amplitudes fluctuate to a certain extent.
(ii) For the cases of low voltage driving (e.g. 20 V), the step fluctuation is small, and the reason lies in that the driving force mainly overcomes the static friction force. While for the cases of high voltage driving (e.g. 80 V), the step fluctuation is increased, and the reason is the alternating static and dynamic frictions.
(iii) Under the same driving frequency, the step increases with the increase of driving voltage amplitude .
(iv) The maximum step obtained by the designed actuator is 0.071 mm when the driving frequency is 550 Hz with the voltage amplitude of 80 V.

According to Fig. 13(b), it can be found that,

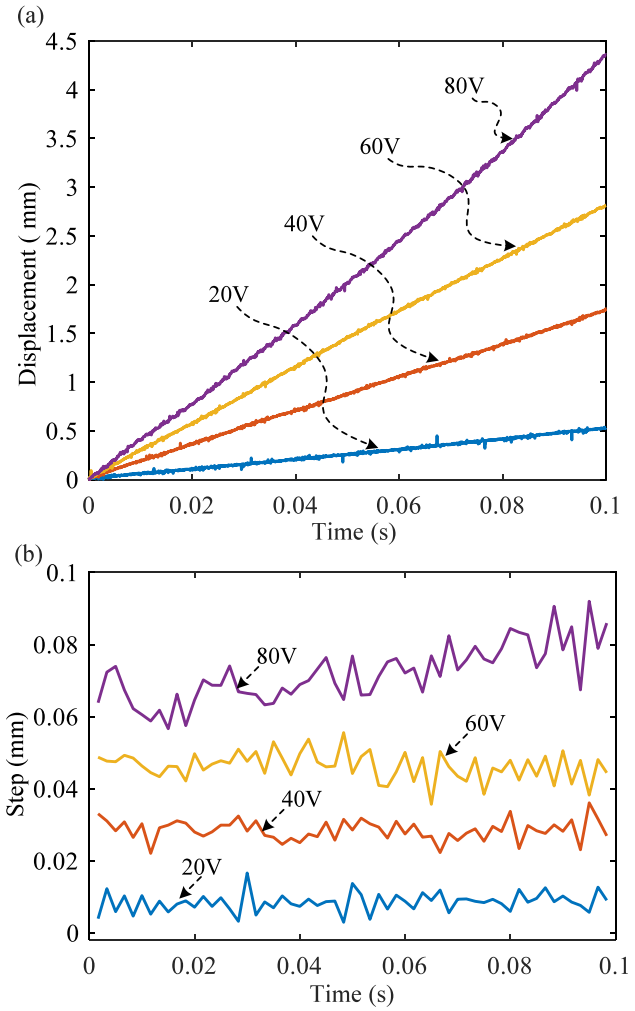

Fig. 14. Test results of output displacement and step size under the driving frequency of 600 Hz. (a) Time–displacement Curve. (b) Time–step Curve.

(i) The driving speed increases first and then decreases at each driving voltage amplitude, reaching the maximum value at 650 Hz.
(ii) The driving speed increases with the increase of voltage under the same driving frequency.
(iii) The maximum speed of the actuator is 44.69 mm/s when the driving frequency is 650 Hz with the driving voltage of 80 V.

5.3. Stepping stability

Driving stability is another important aspect to evaluate the driving performances of an actuator. Fig. 14 shows the time history curve of the displacement and the step of the output shaft when the driving frequency is 600 Hz. It can be seen that the output displacement is continuous and stable under each driving voltage amplitude, and the step is also relatively stable. To be more specific, when the driving voltage is 80 V at 600 Hz, the average step is 71.9 μm with a standard deviation of 6.1 μm.

5.4. Load capacity

In order to test its load capacity, the driving voltage of 80 V at 600 Hz is input to the actuator. The results of driving speed versus load is shown in Fig. 15. It can be seen that the driving speed decreases with the increase of the load. When the load increases from 0 to 60 g, the driving speed decreases from 43.55 mm/s to 6.401 mm/s.

6. Discussions

The partial specifications and performance indexes of the proposed piezoelectric actuator and some stick–slip type or inchworm type actuators in the literature are listed in Tables 4 and 5 to make direct comparisons.

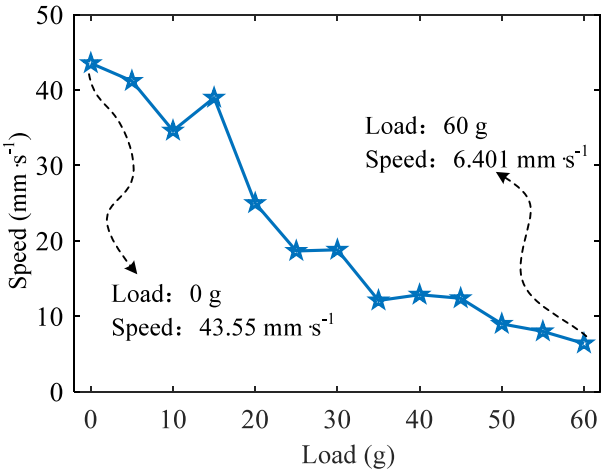

Fig. 15. Test results of output speed under different driving frequencies.

Table 4
Comparisons on specifications with piezoelectric actuators in existing works.

Reference	Size	Material	Directions	Piezo elements
[15]	140 × 100 × 37 mm	65 Mn	Unidirection	1
[16]	32 × 26 × 9 mm	Al 7075	Unidirection	1
[17]	140 × 100 × 74 mm	65 Mn	Unidirection	2
[18]	N/A	N/A	Unidirection	1
[19]	150 × 45 × 30 mm	TC4	Unidirection	3
[20]	84 × 54 × 26 mm	N/A	Unidirection	1
[21]	N/A	Al 7075	Bidirection	2
[24]	N/A	N/A	Bidirection	8
This work	110 × 106 × 10 mm	65 Mn	Bidirection	6

6.1. Specifications

Some remarks can be made as follows according to Table 4.

- **Compactness**: As all the piezoelectric motors in Table 4 consists of compliant hinge mechanisms, compactness is the common advantage of the prototypes. The size of the motor can be properly scaled up or down according the target step size. In addition, the stroke can be extended or lessened by increasing or decreasing the length of the shaft. This is similar to the stick–slip principle based linear motors, where the stroke can be easily changed when using a guide with different length as proposed in [15] for an example.

- **Excitation mode**: Compared with stick–slip type motors (i.e.,[15–17]), the inchworm type motors generally have more piezo elements, thus the excitation signal sequences are a bit more complicated, which puts forward higher requirements of the driving hardware conditions. However, the inchworm type motors can be normally designed as bidirectional. This can be realized by changing the excitation signal sequences as more degrees of freedom of control ports are introduced by more piezo elements. Compared with the same type motor in [21], the proposed motor has more piezo elements while achieves much higher speed.

6.2. Performances

Some remarks can be made as follows according to Table 5.

- **Frequency and Voltage**: Generally, the stick–slip type actuators have larger natural frequencies than those of an inchworm type. For the proposed actuator, the natural frequency is improved significantly among the models of the inchworm type. Thus, the maximum driving speed significantly greater than that of other inchworm type actuators in the literature can be obtained by increasing the driving frequency at a relatively low driving voltage.

- **Speed**: The output speed is a product of step and driving frequency. As for the step size, as stated in Section 5.2, the step of the actuator refers to the displacement of the output shaft in one driving cycle. It is affected by the magnification ratio from

Table 5
Comparisons on performances with piezoelectric actuators in existing works.

Reference	Type	Driving frequency	Voltage	Speed	Load
[15]	Stick–slip	3500 Hz	80 V	46.67 mm/s	40 N
[16]	Stick–slip	415 Hz	100 V	18.84 mm/s	360 g
[17]	Stick–slip	400 Hz	75 V	1.42 mm/s	N/A
[18]	Inchworm	3.2 Hz	75 V	0.77 μm/s	N/A
[19]	Inchworm	50 Hz	120 V	0.72 mm/s	N/A
[20]	Inchworm	40 Hz	150 V	1.2 μm/s	1100 g
[21]	Inchworm	20 Hz	140 V	0.216 mm/s	1.2 N
[24]	Inchworm	10 Hz	100 V	0.412 mm/s	N/A
This work	Inchworm	650 Hz	80 V	44.69 mm/s	60 g

the piezo actuation to the shaft. Hence, the amplitude of the driving voltage and the displacement amplification ratio of the driving mechanism are the two main factors for achieved step size. As for the driving frequency, as stated in Section 4.2, the maximum driving frequency is limited by the first vibrational reso-nance of the driving mechanism. In addition, the complexity of the driving signals limits the driving frequency for that the transient phase among one driving period will lead to poor dynamic performance. Here, the complexity of the driving signals not only relates to the piezo elements but also relates to the excitation mode. In this work, we simplified the excitation mode by adopting the asymmetric driving and clamping configuration. Compared with the same type actuator, the proposed one is obviously superior to others in terms of the maximum output speed. In addition, a maximum speed at a near level can be obtained with much lower driving frequency under the same voltage can be achieved by the proposed actuator when compared with the stick–slip type in [15].

- **Load**: It should be noted that most of the existing literatures (e.g., [16,20,21]) measure the maximum load by increasing the load to reduce the speed of the actuator to 0. However, the maximum load without output speed has little practical significance. Thus, in this work, tests of the driving speed under the loads are performed. The speed with 60 g load can also be 6.401 mm/s, whereas the speed of [15] is 0.7 mm/s under the maximum load. Hence, compared with the maximum speed under no load in some literatures, the proposed actuator still has some advantages.

6.3. Limitations

As mentioned in the introduction, this work sets a symmetrical driving and clamping configuration as a benchmark. An improvement in the excitation signal sequence is realized using the asymmetric driving and clamping configuration. Nevertheless, two limitations can be summarized as:

- The driving complexity can be further simplified with less piezo elements. However, how to maintain the speed and load with the configuration using less piezo elements remains to be a interesting issue.
- The load capacity can be further enhanced. In fact, this is synthetically influenced by the adopted materials, size and structural stiffness. How to make a tradeoff between the target load performance and these factors remains to be another interesting issue.

7. Conclusions

In this work, an improved pusher-type structure of asymmetric driving and clamping configuration along with simplified excitation signal sequences of a high speed piezoelectric actuator is proposed. The left–right asymmetry structure is utilized to simplify the excitation signal sequences. The lever amplification mechanism is designed increase the step, and a hexagonal output shaft is used to enhance the clamping force and to improve the load capacity. Due to the limitation of the working bandwidth, the friction between clamping part and output shaft, the nonlinearity of the piezoelectric stack and so on, it is found that the maximum driving speed increases first and then decreases with the increase of driving frequency, where the optimal driving frequency exists. The obtained maximum driving speed of the actuator is 44.69 mm/s at a driving frequency of 650 Hz with a voltage of 80 V.

Declaration of competing interest

The authors declare that they have no known competing financial interests or personal relationships that could have appeared to influence the work reported in this paper.

Acknowledgments

This work was supported by National Natural Science Foundation of China (Grant Number 51975275), the Jiangsu Provincial Key Research and Development Program, China (Grant No. BE2021034), the Natural Science Foundation of Jiangsu Province, China (Grant No. BK20210294), National Key Laboratory of Science and Technology on Helicopter Transmission, China (Grant No. HTL-A-22G03) and the Postgraduate Research and Practice Innovation Program of Jiangsu Province, China (Grant No. SJCX20_0066).

References

[1] M. Salim, D. Salim, D. Chandran, H.S. Aljibori, A.S. Kherbeet, Review of nano piezoelectric devices in biomedicine applications, J. Intell. Mater. Syst. Struct. 29 (10) (2018) 2105–2121.

[2] J.Y. Lau, W. Liang, K.K. Tan, Motion control for piezoelectric-actuator-based surgical device using neural network and extended state observer, IEEE Trans. Ind. Electron. 67 (1) (2019) 402–412.

[3] J. Yang, Q. Zhang, T. Xu, A novel piezoelectric ceramic actuator with scissoring composite vibration for medical applications, Appl. Sci. 9 (21) (2019) 4637.

[4] H. Elahi, M. Eugeni, P. Gaudenzi, F. Qayyum, R.F. Swati, H.M. Khan, Response of piezoelectric materials on thermomechanical shocking and electrical shocking for aerospace applications, Microsyst. Technol. 24 (9) (2018) 3791–3798.

[5] C.W. Park, B.U. Im, S.J. Shin, B.S. Yoon, J.W. Park, K.J. Yoon, Numerical and experimental analyses of a smart fin using piezoelectric actuator, J. Aircr. 55 (5) (2018) 1817–1830.

[6] E. Villeneuve, C. Volat, S. Ghinet, Numerical and experimental investigation of the design of a piezoelectric de-icing system for small rotorcraft part 2/3: investigation of transient vibration during frequency sweeps and optimal piezoelectric actuator excitation, Aerospace 7 (5) (2020) 49.

[7] W. Xu, Y. Wu, Piezoelectric actuator for machining on macro-to-micro cylindrical components by a precision rotary motion control, Mech. Syst. Signal Process. 114 (2019) 439–447.

[8] R.-J. Li, Y.-J. Lei, L.-S. Zhang, K.-C. Fan, Z.-Y. Cheng, P.-H. Hu, Low-frequency micro/nano-vibration generator using a piezoelectric actuator, in: Engineering for a Changing World: Proceedings; 59th IWK, Vol. 59, Ilmenau Scientific Colloquium, Technische UniversitäT Ilmenau, September 11-15, 2017, (1.1. 13) 2017.

[9] X. Chen, C.-Y. Su, Z. Li, F. Yang, Design of implementable adaptive control for micro/nano positioning system driven by piezoelectric actuator, IEEE Trans. Ind. Electron. 63 (10) (2016) 6471–6481.

[10] M. Habibi, D. Hashemabadi, H. Safarpour, Vibration analysis of a high-speed rotating GPLRC nanostructure coupled with a piezoelectric actuator, Eur. Phys. J. Plus 134 (6) (2019) 307.

[11] C. Liang, F. Wang, B. Shi, Z. Huo, K. Zhou, Y. Tian, D. Zhang, Design and control of a novel asymmetrical piezoelectric actuated microgripper for micromanipulation, Sensors Actuators A 269 (2018) 227–237.

[12] A. Safa, R.Y. Abdolmalaki, S. Shafiee, B. Sadeghi, Adaptive nonsingular terminal sliding mode controller for micro/nanopositioning systems driven by linear piezoelectric ceramic motors, ISA Trans. 77 (2018) 122–132.

[13] C. Sugino, S. Leadenham, M. Ruzzene, A. Erturk, An investigation of electroelastic bandgap formation in locally resonant piezoelectric metastructures, Smart Mater. Struct. 26 (5) (2017) 055029.

[14] Z. Wen, Q. He, G. Qiao, An insight into the flexible drive mechanism in short cylinder ultrasonic piezoelectric vibrator, Rev. Sci. Instrum. 91 (5) (2020) 055003.

[15] Y. Zhang, Y. Peng, Z. Sun, H. Yu, A novel stick–slip piezoelectric actuator based on a triangular compliant driving mechanism, IEEE Trans. Ind. Electron. 66 (7) (2018) 5374–5382.

[16] X. Zhang, Y. Yu, Q. Gao, G. Qiao, Z. Li, X. Lu, T. Cheng, A stick-slip linear piezoelectric actuator with mode conversion flexible hinge driven by symmetrical waveform, Smart Mater. Struct. 29 (5) (2020) 055035.

[17] C. Qiu, J. Ling, Y. Zhang, M. Ming, Z. Feng, X. Xiao, A novel cooperative compensation method to compensate for return stroke of stick-slip piezoelectric actuators, Mech. Mach. Theory 159 (2021) 104254.

[18] R. Wang, Y. Hu, D. Shen, J. Ma, J. Li, J. Wen, A novel piezoelectric inchworm actuator driven by one channel direct current signal, IEEE Trans. Ind. Electron. 68 (3) (2020) 2015–2023.

[19] H. Dong, T. Li, Z. Wang, Y. Ning, Design and experiment of a piezoelectric actuator based on inchworm working principle, Sensors Actuators A (2020) 111950.

[20] Y. Gao, J. Wen, J. Ma, Y. Zhang, R. Wang, Y. Hu, J. Li, A self-adapting linear inchworm piezoelectric actuator based on a permanent magnets clamping structure, Mech. Syst. Signal Process. 132 (2019) 429–440.

[21] Y. Wang, P. Yan, A novel bidirectional complementary-type inchworm actuator with parasitic motion based clamping, Mech. Syst. Signal Process. 134 (2019) 106360.

[22] C. Zhao, Ultrasonic Motors: Technologies and Applications, Springer Science & Business Media, 2011.

[23] P.E. Tenzer, R.B. Mrad, A systematic procedure for the design of piezoelectric inchworm precision positioners, IEEE/ASME Trans. Mechatronics 9 (2) (2004) 427–435.

[24] S. Hua, G. Liu, X. Wang, Y. Wang, J. Li, A piezoelectric inchworm actuator with bidirectional thrust force, Sensors Transducers 171 (5) (2014) 169.

[25] F. Wang, C. Liang, Y. Tian, X. Zhao, D. Zhang, Design of a piezoelectric-actuated microgripper with a three-stage flexure-based amplification, IEEE/ASME Trans. Mechatronics 20 (5) (2014) 2205–2213.